Modeling viscosity of (Mg,Fe)O at lowermost mantle conditions

R. Reali[a,*], J.M. Jackson[b], J. Van Orman[c], D.J. Bower[d], P. Carrez[a], P. Cordier[a]

[a] *Université de Lille, CNRS, INRA, ENSCL, UMR 8207 – UMET – Unité Matériaux et Transformations, F-59000 Lille, France*
[b] *Seismological Laboratory, Division of Geological and Planetary Sciences, California Institute of Technology, Pasadena, CA 91125, USA*
[c] *Department of Earth, Environmental and Planetary Sciences, Case Western Reserve University, Cleveland, OH 44106, USA*
[d] *Center for Space and Habitability, University of Bern, Gesellschaftsstrasse 6, 3012 Bern, Switzerland*

ABSTRACT

The viscosity of the lower mantle results from the rheological behavior of its two main constituent minerals, aluminous (Mg,Fe)SiO$_3$ bridgmanite and (Mg,Fe)O ferropericlase. Understanding the transport properties of lower mantle aggregates is of primary importance in geophysics and it is a challenging task, due to the extreme time-varying conditions to which such aggregates are subjected. In particular, viscosity is a crucial transport property that can vary over several orders of magnitude. It thus has a first-order control on the structure and dynamics of the mantle.

Here we focus on the creep behavior of (Mg,Fe)O at the bottom of the lower mantle, where the presence of thermo-chemical anomalies such as ultralow-velocity zones (ULVZ) may significantly alter the viscosity contrast characterizing this region. Two different iron concentrations of (Mg$_{1-x}$Fe$_x$)O are considered: one mirroring the average composition of ferropericlase throughout most of the lower mantle (x = 0.20) and another representing a candidate magnesiowüstite component of ULVZs near the base of the mantle (x = 0.84). The investigated pressure-temperature conditions span from 120 GPa and 2800 K, corresponding to the average geotherm at this depth, to core-mantle boundary conditions of 135 GPa and 3800 K.

In this study, dislocation creep of (Mg,Fe)O is investigated by dislocation dynamics (DD) simulations, a modeling tool which considers the collective motion and interactions of dislocations. To model their behavior, a 2.5 dimensional dislocation dynamics approach is employed. Within this method, both glide and climb mechanisms can be taken into account, and the interplay of these features results in a steady-state condition. This allows the retrieval of the creep strain rates at different temperatures, pressures, applied stresses and iron concentrations across the (Mg,Fe)O solid solution, providing information on the viscosity for these materials.

A particularly low viscosity is obtained for magnesiowüstite with respect to ferropericlase, the difference being around 10 orders of magnitude. Thus, the final section of this work is devoted to the assessment of the dynamic implications of such a weak phase within ULVZs, in terms of the viscosity contrast with respect to the surrounding lowermost mantle.

1. Introduction

The Earth's core-mantle boundary (CMB) is a major thermochemical boundary layer within the Earth, exerting a primary influence on the evolution of the planet. Seismic observations indicate a significant complexity in this boundary region, including structures of varying length scales and velocity perturbations. In particular, patches near the CMB have been identified, ranging from a few to tens of km thick and ~100 km across, in which the seismic wave velocities are reduced by about 5 to 30% (*e.g.*, Garnero and Helmberger, 1995; Revenaugh and Meyer, 1997; Rost et al., 2006; Hutko et al., 2009; Rost, 2013; Sun et al., 2013; Thorne et al., 2013; Gassner et al., 2015; Frost et al., 2018;

Zhang et al., 2018; see Yu and Garnero, 2018 for a recent review). These ultralow-velocity zones (ULVZs) have been interpreted as aggregates of partially molten material or as solid, iron-enriched assemblages, typically based on proposed sources of velocity reduction (Knittle and Jeanloz, 1991a; Williams and Garnero, 1996; Mao et al., 2004; Labrosse et al., 2007; Sakai et al., 2010; Wicks et al., 2010; Dorfman and Duffy, 2014; Muir and Brodholt, 2015; Liu et al., 2017).

It is suggested that more extreme chemical heterogeneity, such as Fe-rich (Mg,Fe)O or magnesiowüstite residuum from large-scale melting events in Earth's history (Labrosse et al., 2007) may be at least partially responsible for explaining ULVZs (Wicks et al., 2010; Bower et al., 2011; Muir and Brodholt, 2015; Wicks et al., 2017).

* Corresponding author at: Université de Lille, Unité Matériaux et Transformations (UMET) – CNRS UMR 8207 – Bat C6, 59655 Villeneuve d'Ascq Cedex, France.
E-mail address: riccardo.reali@ed.univ-lille1.fr (R. Reali).

Interpretation of these features and the dynamic processes that shape them requires knowledge of their rheological properties. In particular, Bower et al. (2011) presented a geodynamic and mineral physics model of a solid-state ULVZ by exploring the steady-state morphology of a magnesiowüstite-bearing layer at the base of the mantle. Implemented as a chemical density anomaly defined by variable proportions of magnesiowüstite co-existing with bridgmanite, the layer was relatively well constrained in terms of its equation of state. However, one of the least constrained variables in dynamic modeling is the viscosity of the system. In Bower et al. (2011), the viscosity of the system was prescribed only as a function of temperature. While recent progress has been made in estimating the rheological properties of MgO and magnesium-rich (Mg,Fe)O under lower mantle conditions (*e.g.*, Yamazaki and Karato, 2001; Van Orman et al., 2003; Lin et al., 2009; Cordier et al., 2012; Marquardt and Miyagi, 2015; Deng and Lee, 2017; Immoor et al., 2018), no such studies exist for magnesiowüstite.

In this study, we apply the recent development of numerical modeling of dislocation creep based on 2.5D dislocation dynamics to the rheology of iron-rich (Mg,Fe)O magnesiowüstite at the *PT* conditions of the CMB. Since high-temperature creep significantly depends on diffusion, we first present a critical assessment and evaluation of this parameter for (Mg,Fe)O under the conditions of the CMB. Then dislocation dynamics simulations of creep are performed. Using our results of strain rates as a function of the applied stresses, we obtain the effective viscosity of magnesiowüstite. For comparison, we also perform these simulations for ferropericlase. Our results point to very low values of viscosity for magnesiowüstite. These findings motivate the final section of this paper, where we assess the influence of low viscosity magnesiowüstite on the dynamics of the lowermost mantle by re-visiting the framework presented in Bower et al. (2011).

2. Method: 2.5D dislocation dynamics

2.5–dimensional (2.5D) dislocation dynamics (DD) is now a well–established numerical tool which considers the collective motions and interactions of dislocations at the mesoscale. It has been first developed to model creep in aluminum (Keralavarma et al., 2012) and then applied to olivine (Boioli et al., 2015a,b) and MgO (Reali et al., 2017). It is therefore a viable instrument to model creep of (Mg,Fe)O at high pressures and temperatures.

A full description of the 2.5D-DD simulation technique adopted in this study along with a comparison with other methods employing dislocation dynamics is provided in previous work (Reali et al., 2017). There, the model was benchmarked for MgO at ambient conditions with respect to experimental and other numerical data, demonstrating its validity in a variety of thermal regimes. In particular, at high temperatures, by combining dislocation glide together with dislocation climb, this approach could satisfactorily reproduce the existing creep data on MgO. In fact, when at high temperatures diffusion is active, dislocations can escape their glide planes by climb. Dislocations in a dipole configuration may consequently approach each other until they reach a given critical distance and annihilate. Hence, the dislocation density is controlled by the interplay between dislocation multiplication and dislocation annihilation promoted by climb. This leads to a steady-state regime where, with respect to time, the dislocation density fluctuates around an equilibrium value and the plastic strain increases linearly. In this condition, the rate of creep strain as a function of applied stress and temperature can be described using a power law creep equation, in good agreement with experimental data. Here we focus on this high temperature regime (above approximately half of the melting temperature) at lowermost mantle conditions. In this regime, temperatures are high enough to favor diffusion and consequently render dislocation climb, which is diffusion–dependent, a viable recovery mechanism. The main features of the model in this regime are outlined below.

Dislocation dynamics is based on continuum elasticity theory, which describes the elastic field induced by dislocations in a crystal,

and the interactions of dislocations with each other and with the stress field resulting from an external, deviatoric loading. The 2.5D–DD formulation for this work considers a simplified 2D framework in which local rules are taken into account in order to mimic relevant 3D mechanisms, such as dislocation multiplication, annihilation and junction formation (Benzerga et al., 2003; Gómez-García et al., 2006; Durinck et al., 2007). Subsequently, these features were tested on olivine by Boioli et al. (2015a,b) and on MgO by Reali et al. (2017), which provides more details on the adjustment of these parameters. This 2.5D formulation allows the construction of a simple model that captures the most important 3D dislocation mechanisms and readily includes the interplay between glide and climb in high temperature, high pressure creep conditions.

Throughout most of the lower mantle, the magnesium-iron oxide in equilibrium with calcium silicate perovskite and bridgmanite is thought to be magnesium-rich (Mg,Fe)O ferropericlase, which exhibits the B1 rock-salt structure with space group $Fm\bar{3}m$. Ferrous iron in ferropericlase undergoes a gradual spin pairing transition, which is completed by the *PT* conditions of the base of the mantle (Sturhahn et al., 2005; Tsuchiya et al., 2006). In addition to the temperature dependence, the pressure of the spin pairing transition, as well as the width (pressure range), increases with increasing iron concentration (*e.g.*, Solomatova et al., 2016). Although studies indicate that the iron cations in iron-rich (Mg,Fe)O begin to pair at pressures of around 120 GPa and 300 K (*e.g.*, Speziale et al., 2005; Wicks et al., 2010; Fischer et al., 2011; Ozawa et al., 2011), the presence of magnesium widens the pressure-temperature stability field of the B1 structure compared to FeO (Wicks et al., 2015). Thus, thermal effects and the presence of a small amount of magnesium would likely prohibit a spin crossover in iron-rich (Mg,Fe)O at CMB conditions. Therefore, in this study, we consider high–spin magnesiowüstite $(Mg_{0.16}Fe_{0.84})O$ and low–spin ferropericlase $(Mg_{0.80}Fe_{0.20})O$ to represent possible end–member cases of (Mg,Fe)O at lowermost mantle conditions. For these compositions, and for a sake of comparison, we consider two *PT* conditions: one resembling the geotherm at 120 GPa and 2800 K and the other representing CMB conditions suitable for solid–state ULVZs, at 135 GPa and 3800 K. Additionally, in order to have a first estimate of the creep activation enthalpy for magnesiowüstite at CMB conditions, another set of calculations were run at 135 GPa and 3200 K.

The elastic properties for high–spin magnesiowüstite are taken from experimental results of Wicks et al. (2015, 2017), which constrained the thermal equation of state and shear elastic properties for this phase under lowermost mantle conditions using powder X–ray diffraction and inelastic X–ray scattering techniques. The elastic properties for low–spin ferropericlase are taken from a theoretical study that investigated the thermoelastic effects related to the spin crossover up to pressures of 130 GPa and 4000 K (Wu and Wentzcovitch, 2014). We provide the elastic properties used for these two end–member cases along with their lattice constant and burgers vector magnitude in Table 1.

In our simulations, 200 to 400 dislocations having Burgers vectors $b = \frac{1}{2}\langle 1\,1\,0 \rangle$ are introduced in a simulation cell having edges of ~ 10–$60\,\mu m$. These dislocations are allowed to glide in two slip systems belonging to the easiest slip family – *i.e.* $\frac{1}{2}\langle 1\,1\,0 \rangle\{1\,1\,0\}$. The cell is a square of size $L_x = L_y$ and dislocation lines are introduced as straight segments of constant length $L = 1\,\mu m$ perpendicular to the reference plane, where both glide and climb directions lie. All dislocation lines have edge character, which is the limiting feature concerning dislocation climb. The dislocation climb direction is perpendicular to the glide direction. Deviatoric stress is applied in order to symmetrically load the two slip systems, resulting in an equal Schmid factor of 0.433 for both of them (Reali et al., 2017). Dislocations gliding in different planes may cross each other and form junctions which are oriented along the direction of intersection between the two planes. Here, we consider two glide planes that form an angle of 120 degrees with each other, allowing for the formation of stable, sessile junctions (Carrez et al., 2005).

Table 1
Lattice constant, ½⟨1 1 0⟩ Burgers vector magnitude, elastic properties and estimated liquidus temperatures for $(Mg_{0.16}Fe_{0.84})O$ magnesiowüstite and $(Mg_{0.80}Fe_{0.20})O$ ferropericlase at the pressure and temperature conditions of interest. [a]Wicks et al. (2015, 2017), [b]Wu and Wentzcovitch (2014) extrapolated to 135 GPa, [c]Values are taken as a linear interpolation between the melting points of MgO and FeO (Cohen and Weitz 1998; Fat'yanov and Asimow, 2014; Fischer and Campbell 2010). See text for details.

	$(Mg_{0.16}Fe_{0.84})O$[a]			$(Mg_{0.80}Fe_{0.20})O$[b]	
	120 GPa, 2800 K	135 GPa, 3200 K	135 GPa, 3800 K	120 GPa, 2800 K	135 GPa, 3800 K
Lattice constant a (Å)	3.83	3.81	3.82	3.86	3.87
Burgers vector b (Å)	2.71	2.69	2.70	2.73	2.74
Density (g/cm^3)	7.90	8.03	7.97	5.38	5.36
V_S (km/s)	3.50	3.52	3.47	7.16	7.09
V_P (km/s)	8.20	8.19	8.14	13.58	13.79
Poisson ratio	0.39	0.39	0.39	0.31	0.32
Shear Modulus μ (GPa)	97	100	96	276	270
Bulk Modulus (GPa)	402	406	401	625	660
Liquidus (K)[c]	4300	4440	4440	7220	7410

For all the tested *PT* conditions, a constant creep stress σ ranging from 10 to 50 MPa was applied to the simulated system. Furthermore, in the case of $(Mg_{0.80}Fe_{0.20})O$ ferropericlase, some tests were run also at higher stresses, up to 500 MPa, in order to better anchor the fit for the strain rate as a function of stress. In fact, since climb in $(Mg_{0.80}Fe_{0.20})O$ ferropericlase is very slow for many of the *PT* conditions considered, it was possible to achieve a minimum acceptable strain of around 1% in practical times only by raising the applied stress. At steady–state, the equilibrium dislocation density, equal to the number of dislocations in the system divided by its area, rises with the applied, constant creep stress. Therefore, the cell size was adjusted in order to have a representative and comparable number of dislocations at equilibrium for all the tested stresses. Equilibrium dislocation densities in this study varied between 10^{11} and 10^{13} m^{-2}, requiring cell dimensions $L_x = L_y$ from 8 to 60 μm.

A key point in modeling dislocation creep is the description of the interplay between a strain–producing mechanism and a recovery mechanism, which controls the time scale at which the deformation is taking place. Here, athermal dislocation glide is the strain producing mechanism. The recovery mechanism (dipole annihilation) is controlled by dislocation climb, which allows the dislocation to move outside its glide plane through the absorption or emission of a formula unit to or from the dislocation line.

At the temperatures considered here, thermal activation is sufficient to overcome lattice friction. Thus, plastic shear is athermal and constrained by the interactions between dislocations. In this regime, dislocations move by glide at a free flight velocity v_{ath} described by a viscous drag equation:

$$v_{ath} = \frac{b\tau}{B_v} \tag{1}$$

where b is the Burgers vector, τ is the effective resolved shear stress acting on the dislocation and B_v is a viscous drag coefficient that varies linearly with temperature (Hirth and Lothe, 1992). In particular, $\tau = \tau_{app} + \tau_{int}$ is calculated at each dislocation position and represents the sum of the applied stress τ_{app} and the elastic interaction stress τ_{int} induced by all the other dislocations, both projected along the slip direction. An experimental estimate of B_v for (Mg,Fe)O is lacking, therefore a value measured on other fcc oxides at 300 K is taken from the literature (Singh et al., 2008) and is scaled to the considered temperatures (*i.e.* from 2800 to 3800 K). The free–flight mobility law is not expected to play a relevant role in simulations describing plasticity in this regime (Amodeo et al., 2014) because the average velocity of dislocations in the microstructure is limited by their forest interactions (*i.e.*

dislocation–dislocation contact reactions). For this reason, the forest obstacles control the plastic flow and in the present model they are represented by dislocation junctions, which are formed when two attractive dislocations gliding in different planes come to a distance smaller than the average length of junctions under stress, which is estimated from 3D simulations (Devincre et al., 2006). In this case, dislocation positions are locked and the interaction stress between them is set to zero. The junction will remain stable as long as the stress on each dislocation composing it, evaluated similarly to τ in Eq. (1), is lower than a critical value. If this value is exceeded, the dislocations composing the junction will be unlocked and made free to move. The local rule to break a junction in a 2.5D–DD model is defined by Gómez-García et al. (2006) and was tuned for MgO by Reali et al. (2017).

The other important mobility law is the one describing dislocation climb, which allows dislocations stuck in a minimum energy configuration to escape their glide plane and eventually interact and annihilate with other segments. Climb is the recovery mechanism which counterbalances the athermal, forest dislocation glide mechanism (in turn responsible for dislocation multiplication) and brings the system to the steady–state creep regime. Climb takes place through the self--diffusion of defects, mainly vacancies, which are adsorbed or emitted by the dislocation line. Climb controls the dynamics of the entire creep process, under the assumption that the dislocation lines are saturated with jogs (*i.e.*, steps on the dislocation line in the climb direction). Therefore, under these conditions, vacancies are adsorbed or emitted instantaneously. At the steady–state, the dislocation climb velocity v_c can be expressed following the Hirth and Lothe (1992) and Caillard and Martin (2003) formulation:

$$v_c = \alpha \frac{D^{sd}}{b} \left[exp\left(\frac{\tau_c \Omega}{k_B T} \right) - \frac{c_\infty}{c_0} \right] \tag{2}$$

where τ_c is the climb stress, calculated similarly to τ but resolved along the climb direction, T is the temperature and k_B the Boltzmann constant. $\alpha = 2\pi/\ln(R/r_c)$ is a geometrical factor that describes the cylindrical geometry of the vacancy flux field around the dislocation line, where R and r_c represent the two radii of the cylindrical surfaces through which the vacancy flux is calculated. r_c is the dislocation core radius and R is taken as a fraction of the average dislocation distance. Being within the logarithmic term, the R/r_c ratio does not significantly affect the climb velocity values and here is taken constant and equal to 100 (Boioli et al., 2015a,b). Ω is the formation volume of vacancies in the cation and O sites and is calculated from the unit cell volume of (Mg,Fe)O – *i.e.* $\Omega = a^3/Z$ where $Z = 4$ is the number of formula units

per unit cell. c_∞ and c_0 are the vacancy concentrations far from the dislocation and the equilibrium vacancy concentration in the bulk volume, respectively. Following Boioli et al. (2015a), we assume that far away from the dislocations the vacancy concentration is constant and equal to the equilibrium concentration in the bulk volume ($c_\infty = c_0$). Finally, D^{sd} is the vacancy self–diffusion coefficient which controls the flow of atomic species from and to the climbing dislocation. Thus, this parameter is of considerable importance, since it is the one that ultimately controls the strain–rate. Self–diffusion is described by an Arrhenius–type formula:

$$D^{sd} = D_{Ox} = D_0 \, exp\left(-\frac{\Delta H^{sd}}{k_B T}\right) \tag{3}$$

where D_0 is a pre–exponential factor and ΔH^{sd} is the activation enthalpy for oxygen self–diffusion which is the sum of the vacancy formation and migration enthalpy. As will subsequently be shown, the climb–limiting species in (Mg,Fe)O is oxygen, and therefore it is necessary to properly estimate D_{Ox} for (Mg,Fe)O as a function of composition at CMB conditions.

3. Evaluation of high pressure and high temperature self–diffusion coefficients of (Mg,Fe)O

Self–diffusion of MgO has been extensively studied over the past decades, for both the cation and anion sublattices. However, a full description of this phenomenon as a function of pressure, temperature and composition for lowermost mantle conditions is lacking. Therefore, it is necessary to develop a method to conveniently estimate diffusion coefficients to be introduced into the 2.5D dislocation dynamics model.

Concerning the magnesium sublattice in periclase, it can be stated that extrinsic cation vacancies control Mg self–diffusion at any temperature up to the melting point. This is because aliovalent positively charged solutes like Fe^{3+}, Al^{3+} and Cr^{3+} tend to be present at concentrations much higher than the intrinsic vacancy concentrations, even in nominally pure synthetic crystals. The presence of aliovalent solutes leads to the formation of cation vacancies, to maintain charge balance, and hinders the formation of oxygen vacancies, which also have a net positive charge. For this reason, oxygen self–diffusion coefficients are at least 2–3 orders of magnitude smaller than those of magnesium at any investigated temperature (Van Orman and Crispin, 2010 and references therein). Oxygen self–diffusion D_{Ox} is thus considered as the rate–limiting mechanism for dislocation climb.

A review of the literature on oxygen self–diffusion coefficients in MgO at ambient conditions (Van Orman and Crispin, 2010) shows that at high temperatures an activation energy resembling that of the intrinsic regime is observed in some cases, while a phenomenon with smaller temperature dependence is often observed at lower temperatures. Self–diffusion in the latter case appears to be strongly influenced by structural defects, but not by chemical impurities (*e.g.* Yang and Flynn, 1994, 1996), and is consistent with fast transport along dislocation cores (Van Orman and Crispin, 2010).

Although fast transport via dislocations may have an important role in the bulk diffusivity of oxygen in both experimental and natural samples, this process is not relevant to dislocation climb. The latter refers to the net flux of vacancies from and to the dislocation line across a cylindrical surface, which excludes the core–related effects and therefore does not consider the aforementioned, structure–sensitive factors affecting diffusion (*cf.* the definition of the geometrical parameter α in the climb velocity law, Eq. (2)). Therefore, the starting point for the evaluation of diffusion at lower mantle conditions is the assumption that oxygen diffusion is intrinsic.

Experimental measurements indicate that oxygen diffusion coefficients are insensitive to the concentration of aliovalent dopants, either in the intrinsic regime (Yang and Flynn, 1994, 1996) or in the extrinsic regime controlled by structural defects (Ando et al., 1983).

At high temperatures, as mentioned before, higher activation enthalpies for diffusion are generally observed (Yang and Flynn, 1994, 1996; and Oishi et al., 1983). In particular, Yang and Flynn (1994) found an activation enthalpy in good agreement with the theoretical value for intrinsic oxygen diffusion. Furthermore, the absolute values of the diffusion coefficients determined experimentally by these authors were found to be in good agreement with the theoretical values. As it provides strong experimental evidence for intrinsic diffusion, Yang and Flynn (1994) will be considered as a benchmark at ambient conditions for the calculated high pressure, high temperature diffusion coefficients.

Intrinsic diffusion in MgO under lower mantle conditions was calculated by Ita and Cohen (1997), who used molecular dynamics simulations and found that oxygen–magnesium vacancy pairs would predominate over isolated oxygen vacancies (Schottky defects) at low temperatures, while the opposite was found for temperatures exceeding 1000 K. Nevertheless, we expect small differences between the cases where oxygen diffusion occurs through isolated oxygen vacancies or vacancy pairs, as discussed by Yang and Flynn (1994). In fact, values yielded by Ita and Cohen (1997) are in close agreement with the ones of Yang and Flynn (1994).

Ita and Cohen (1997) also found that the homologous temperature relation works well to describe intrinsic diffusion in MgO:

$$D_{Ox} = D_0 * exp(-g * T_m/T) \tag{4}$$

where T_m is the melting temperature and D_0 and g are empirical constants. This relation also describes the pressure dependence of diffusivity in crystalline metals, as Reaman et al. (2012) showed using diamond anvil cell experiments at pressures up to about 70 GPa. As shown below, the homologous temperature relation also provides a remarkably good description of intrinsic anion diffusion in ionic crystals, with anion diffusion data for a wide range of crystals having the rock salt structure all following a common homologous temperature scaling.

As noted above, aliovalent impurities, including trace levels of iron, have no influence on oxygen diffusion in MgO. However, iron in (Mg,Fe)O has a strong influence on the bond strength, influencing dramatically the melting temperature and, according to the homologous temperature relation, the oxygen diffusion coefficient. Here, we use the homologous temperature relation, fit to anion diffusion data for MgO and other rock-salt structured ionic crystals, to calculate oxygen diffusion coefficients in (Mg,Fe)O as a function of composition, pressure and temperature. To use this relation for (Mg,Fe)O, it is necessary to estimate reasonable values of T_m for magnesiowüstite and ferropericlase (*cf.* Table 1). For a solid solution there is no single value of T_m at a given pressure, and in particular there is a wide gap between the solidus and liquidus curves for (Mg,Fe)O (Wu et al., 1993; Zhang and Fei, 2008). Our estimates for the values of T_m to be used in the homologous temperature relation were calculated as follows. First, we use the melting curve of MgO computed by Cohen and Weitz (1998) up to 100 GPa, because it was determined self–consistently with the diffusion model implemented here (Ita and Cohen, 1997). The MgO melting curve at higher pressures has been constrained using recent shock measurements that places a lower bound melting temperature of 9000 K at 240 GPa (Fat'yanov and Asimow, 2014). Second, we use the FeO end–member melting curve defined by the combined determinations by Fischer and Campbell (2010) to 77 GPa and Kato et al. (2016) to 131 GPa. Third, we assume that the effective T_m values for magnesiowüstite and ferropericlase vary linearly between these two end–members. This is a reasonable first-order approximation, given (1) the large spread in reported high pressure melting temperatures of FeO (Knittle and Jeanloz, 1991b; Shen et al., 1993; Fischer and Campbell, 2010; Komabayashi, 2014; Kato et al., 2016) and MgO (see Fat'yanov and Asimow, 2014 for a review); (2) the large spread in the pressure dependence of the solidus and liquidus curves for the (Mg,Fe)O solid solution (Zerr and Boehler, 1994; Zhang and Fei, 2008; Du and Lee,

Table 2
Oxygen self–diffusion parameters for MgO global fit as a function of pressure and temperature (from Ita and Cohen, 1997).

Equation parameter	Symbol	Value
cubic cell parameter	a	4 Å
attempt frequency	ν	5.2 THz
activation entropy ($P = 0$)	S_0	$4k_B$
S_0 pressure derivative	$S_0^{'}$	0.02 k_B/GPa
activation energy	E_0	$9.4 \cdot 10^{-19}$ J
activation volume ($P = 0$)	V_0	16.7 Å^3
V_0 pressure derivative	$V_0^{'}$	–0.038 Å^3/GPa

2014; Deng and Lee, 2017; Fu et al., 2018); and (3) the lack of empirical evidence that the solidus or liquidus temperature of a solid solution is a better approximation for the effective melting temperature used in the homologous temperature scaling than a linear interpolation of the end-member melting temperatures.

The self–diffusion coefficients to be implemented in the 2.5D-DD code for this study were evaluated starting from the results of Ita and Cohen (1997), which provide an empirical equation expressing the self–diffusion coefficients of Mg and O as a function of pressure and temperature:

$$lnD^{sd}(P,\,T) = ln(a^2\nu) + \frac{S_0 + PS_0^{'}}{k_B} - \frac{E_0 + PV_0 + P^2V_0^{'}}{k_BT} \quad (5)$$

where P is pressure in GPa and T is temperature in K. The other parameters are taken from oxygen self–diffusion data since the anion diffusion represent the slowest mechanism in MgO, and are listed in Table 2.

Starting from this equation it is possible to calculate the oxygen self–diffusion coefficient as a function of temperature for a fixed pressure. This was made for pressures ranging from 100 to 140 GPa and temperatures between 1500 and 4000 K. Each curve was sampled every 100 K and the retrieved values were plotted as a function of the homologous temperature in order to obtain a dataset to be fit with the homologous temperature relation highlighted in Eq. (4).

The obtained dataset along with the relative fit using the homologous temperature relation is showed in Fig. 1, together with other
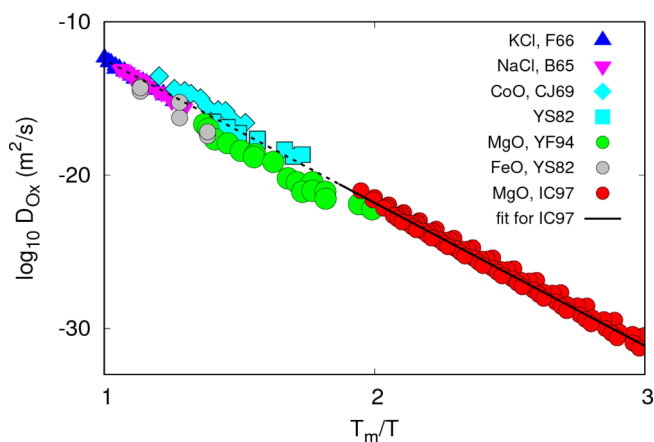

Fig. 1. Oxygen self–diffusion coefficients D_{Ox} as a function of the homologous temperature for different oxides and halides. The high pressure, high temperature numerical data on MgO obtained by Ita and Cohen (1997) (red dots) are fit using the homologous temperature relation described in Eq. (4) (black line), which is in good agreement also with other intrinsic, oxygen self–diffusion experimental data of oxides and halides retrieved from literature. F66: Fuller (1966), B65: Barr et al. (1965), CJ69: Chen and Jackson (1969), YS82: Yamaguchi and Someno (1982), YF94: Yang and Flynn (1994), IC97: Ita and Cohen (1997). (For interpretation of the references to colour in this figure legend, the reader is referred to the web version of this article.)

experimental data on intrinsic anion self–diffusion for oxides and halides from the literature. The agreement between the scaling law adopted in this study and the ambient condition points is remarkable, and indicates that ionic crystals with the rock–salt structure all follow a common homologous temperature relationship with respect to intrinsic diffusion on the anion sublattice. The retrieved values for g and D_0 are 21.5 and $7.2 \cdot 10^{-4}$ m^2/s, respectively.

Substituting T_m of MgO with values for (Mg$_{0.80}$Fe$_{0.20}$)O and (Mg$_{0.16}$Fe$_{0.84}$)O at 120 and 135 GPa allows to calculate the intrinsic oxygen self–diffusion coefficient at a given temperature for the two different compositions. The diffusion coefficients are then evaluated in terms of the more canonical Arrhenius type of relation described in Eq. (3). Thus, the self–diffusion activation enthalpy is equal to:

$$\Delta H^{sd} = g * T_m * k_B \quad (6)$$

while the pre–exponential factor D_0 is the same for Eqs. (3) and (4).

The values obtained from this approach and employed in the present study are shown in Table 3.

4. Dislocation dynamics creep simulations

4.1. Results

The strain evolution as a function of time for magnesiowüstite at the three tested PT conditions is shown in Fig. 2 for all of the considered applied stresses. All the curves correspond to a linear behavior that allows for the determination of the creep strain rate as a function of stress. To further verify that the steady state condition is achieved, we plot the dislocation density as a function of time. This is done in Fig. 3a where the results obtained at 135 GPa and 3800 K are shown. The dislocation densities oscillate around a constant value, demonstrating that dislocation annihilation and multiplication are counterbalancing each other. This means that the coupling of the two mechanisms introduced in the code – *i.e.* dislocation glide and climb – leads to a steady state equilibrium condition and therefore reproduces well the process of creep. Fig. 3b displays the individual contributions of these two mechanisms to the resulting creep strain rate: it is evident that the vast majority of deformation is due to dislocation glide (ε_{glide}), which is a very efficient strain-producing mechanism. Climb, on the other hand, is diffusion-dependent, and therefore has a major control on the evolution of strain with time – *i.e.* it defines the time scale at which the deformation is taking place. In Fig. 2a,b,c this is evident from the different orders of magnitude on the time axes. Given that in this regime dislocation glide is athermal and therefore is not affected by temperature variations, a comparable deformation of 1–2% is achieved for every PT condition. On the other hand, the different temperatures affect the diffusion coefficient, on which the climb velocity is directly dependent (*cf.* Eq. (2)), changing the time control of the dynamics and therefore the rate of deformation.

The results found in this study confirm that this kind of interplay works well to describe creep of (Mg,Fe)O after other studies had confirmed its validity by applying the same method at ambient conditions to olivine (Boioli et al., 2015a,b) and MgO (Reali et al., 2017).

The results for strain as a function of time for ferropericlase (Mg$_{0.80}$Fe$_{0.20}$)O are shown in Fig. 4. As stated above, in this case several tests were run at higher applied stresses – up to 500 MPa – in order to obtain reliable deformations in practical simulation times. Nonetheless, a steady-state condition at the usual stresses from 10 to 50 MPa was verified also for each tested PT condition for ferropericlase.

It is therefore possible to evaluate the creep strain rates from the obtained curves and characterize them using the well established power law type of equation:

$$\dot{\varepsilon} = \dot{\varepsilon_0}\left(\frac{\sigma}{\mu}\right)^n exp\left(-\frac{Q}{k_BT}\right) \quad (7)$$

Table 3

Numerical values for D_{Ox}, ΔH_{sd} and T_m employed in this study for (Mg,Fe)O.

	(Mg$_{0.16}$Fe$_{0.84}$)O			(Mg$_{0.80}$Fe$_{0.20}$)O	
	120 GPa, 2800 K	135 GPa, 3200 K	135 GPa, 3800 K	120 GPa, 2800 K	135 GPa, 3800 K
D_{Ox} (m^2/s)	$3.4 \cdot 10^{-18}$	$8.2 \cdot 10^{-17}$	$9.1 \cdot 10^{-15}$	$6.2 \cdot 10^{-28}$	$4.6 \cdot 10^{-22}$
ΔH_{sd} (eV)	8.0	8.2	8.2	13.4	13.7
T_m (K)	4300	4440	4440	7224	7414
T / T_m	0.7	0.7	0.9	0.4	0.5
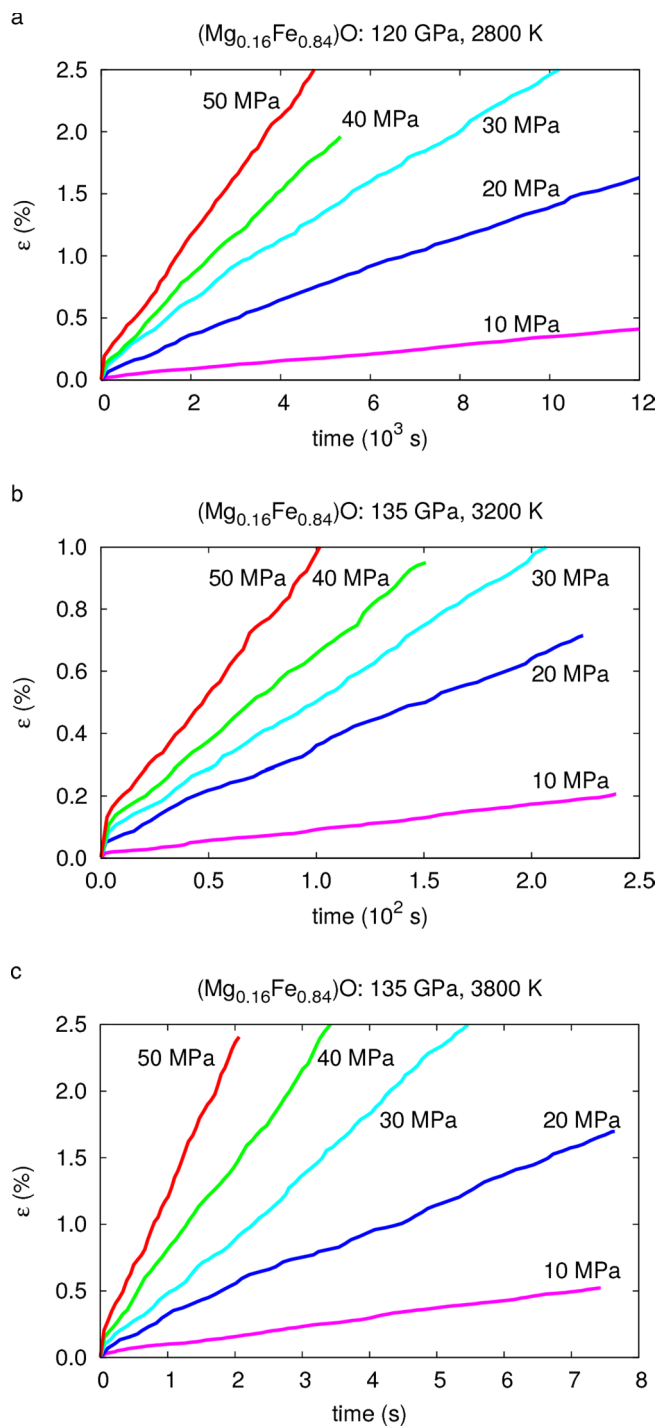
Fig. 2. (Mg$_{0.16}$Fe$_{0.84}$)O magnesiowüstite: plastic strain as a function of time at 2800 K and 120 GPa (a), 3200 K and 135 GPa (b) and 3800 K and 135 GPa (c). The values of the applied, deviatoric stress σ are also shown for each simulation.
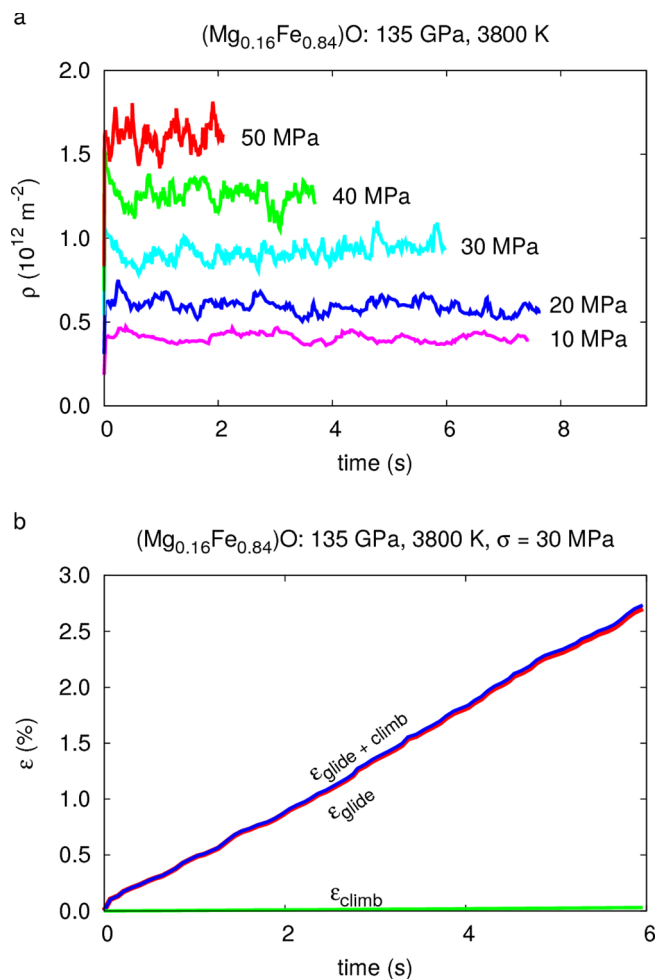

Fig. 3. (Mg$_{0.16}$Fe$_{0.84}$)O magnesiowüstite: evolution of the dislocation density as a function of time in the case at 3800 K and 135 GPa (a) and contribution of glide (ε_{glide}) and climb (ε_{climb}) to the total achieved strain($\varepsilon_{glide+climb}$) (b). In this case the applied stress σ is 30 MPa.

where $\dot{\varepsilon}_0$ is a fitting parameter, σ the applied stress, μ the shear modulus, n the power law stress exponent and Q the creep activation enthalpy.

The strain rates as a function of stress for magnesiowüstite and ferropericlase are shown in Fig. 5. The retrieved average stress exponents are 1.6 for magnesiowüstite and 2.8 for ferropericlase. Regarding the evaluation of the creep activation enthalpy Q only a first attempt could be done for the case of magnesiowüstite at 135 GPa. This is the only case, in fact, where the strain rates could be compared at the same pressure and different temperatures. The obtained average value for Q in this case was 8.0 eV, in fair agreement with the oxygen self-diffusion activation enthalpy ΔH^{sd} previously evaluated for this case (that is, 8.2 eV, *cf.* Table 3). A similar result was also found by Reali et al. (2017) for MgO. Therefore, this finding further confirms how
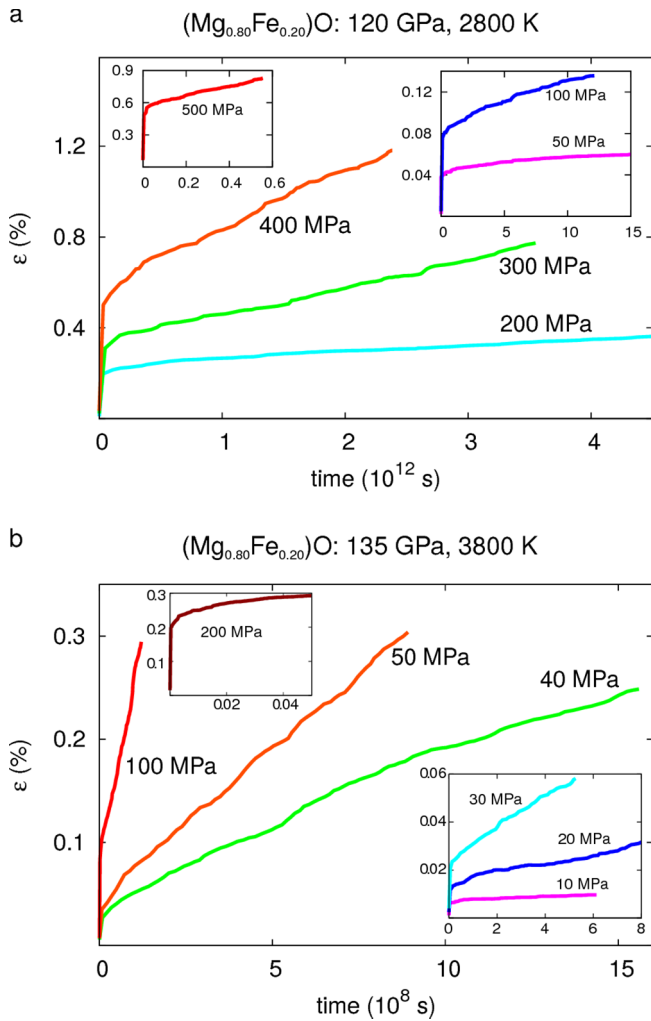
a

b

Fig. 4. $(Mg_{0.80}Fe_{0.20})O$ ferropericlase: plastic strain as a function of time at 2800 K and 120 GPa (a) and at 3800 K and 135 GPa (b). For each graph, the unities of the axes are the same for the main graph and the respective insets.
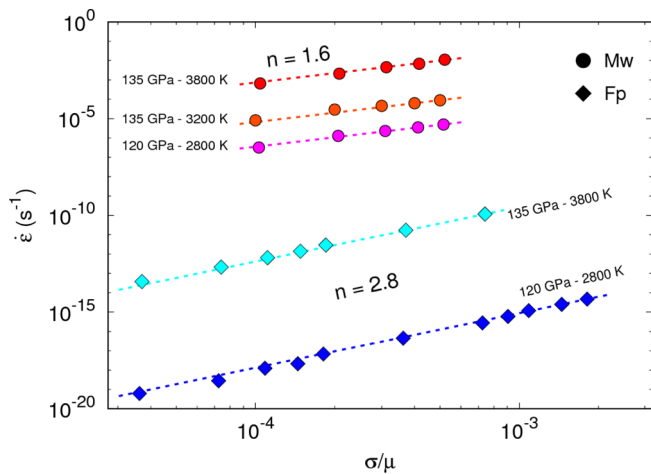

Fig. 5. Creep strain rates as a function of stress (over the shear modulus) of $(Mg_{0.16}Fe_{0.84})O$ magnesiowüstite (Mw) and $(Mg_{0.80}Fe_{0.20})O$ ferropericlase (Fp). The average power law stress exponents n are also displayed for the two phases.

dislocation climb, which is diffusion-dependent, is the mechanism controlling the rate of deformation and therefore creep.

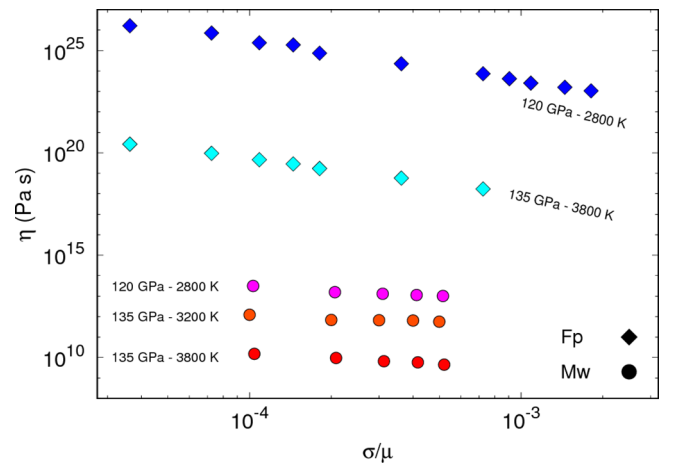Knowing the strain rates it is possible to deduce the viscosity of

Fig. 6. Viscosities as a function of stress (over shear modulus) for $(Mg_{0.16}Fe_{0.84})O$ magnesiowüstite (Mw) and $(Mg_{0.80}Fe_{0.20})O$ ferropericlase (Fp) at core-mantle boundary conditions.

$(Mg,Fe)O$. This is done by considering the effective viscosity η:

$$\eta = \frac{\sigma}{\dot{\varepsilon}} \tag{8}$$

The obtained viscosities for magnesiowüstite and ferropericlase at CMB conditions are shown in Fig. 6.

4.2. Discussion of uncertainties

The major result is the prediction that magnesiowüstite has a viscosity that is reduced by about 10 orders of magnitude relative to ferropericlase at CMB conditions. In support of this general conclusion, we consider some of the uncertainties involved in the methods presented here. One source of uncertainty is the estimate for T_m. A recent study on recovered samples from laser–heated diamond–anvil cell experiments up to 80 GPa suggests significantly low liquidus and solidus temperatures for ferropericlase (Deng and Lee, 2017). If this phenomenon occurs at CMB conditions, this could explain why at upper D″ conditions simulated here (120 GPa and 2800 K), ferropericlase exhibits smaller strain rates (10^{-19} s^{-1}, resulting in higher viscosities) than the expected values for this region (*i.e.* 10^{-16}–10^{-14} s^{-1}), although the value we obtain at lowermost mantle conditions of 135 GPa and 3800 K is comparable (10^{-14} s^{-1}).

Other sources of uncertainty are the elastic properties of $(Mg,Fe)O$ at CMB conditions. In the case of magnesiowüstite, we investigate the influence of increasing the shear modulus by 10% on our results at 135 GPa. By evaluating a stiffer material, we indirectly address two effects: 1) a relatively cooler CMB, 2) uncertainty of the T_m value for Mw. By simulating a stiffer material (cooler CMB), for example, the conditions remain below the solidus of Mw. We find smaller strain rates for the stiffer Mw, varying rather uniformly between 20 and 30%, thus of the same order of magnitude. These results are shown in Fig. 7 and the numerical values of the different strain rates in Table 4.

It is becoming more likely that some ULVZs may represent chemically dense solid–state assemblages and others may indicate the presence of partial melts (*e.g.* Hernlund and Tackley, 2007; Hernlund and Jellinek, 2010; Li et al., 2017). The stable phase assemblage in any particular region is dictated, in part, by phase equilibria and the relationship of the assemblage's solidus to the thermal profile, all of which have relatively large uncertainties in the D″ region (*e.g.* Lay et al., 2008; Zhang and Fei, 2008; Fiquet et al., 2010; Fischer and Campbell, 2010; Andrault et al., 2014; Du and Lee, 2014; Komabayashi, 2014; Nomura et al., 2014; Tateno et al., 2014; Pradhan et al., 2015; Zhang et al., 2016; Deng and Lee, 2017). Combined with previous reports on the sound velocities of magnesiowüstite that implicate its
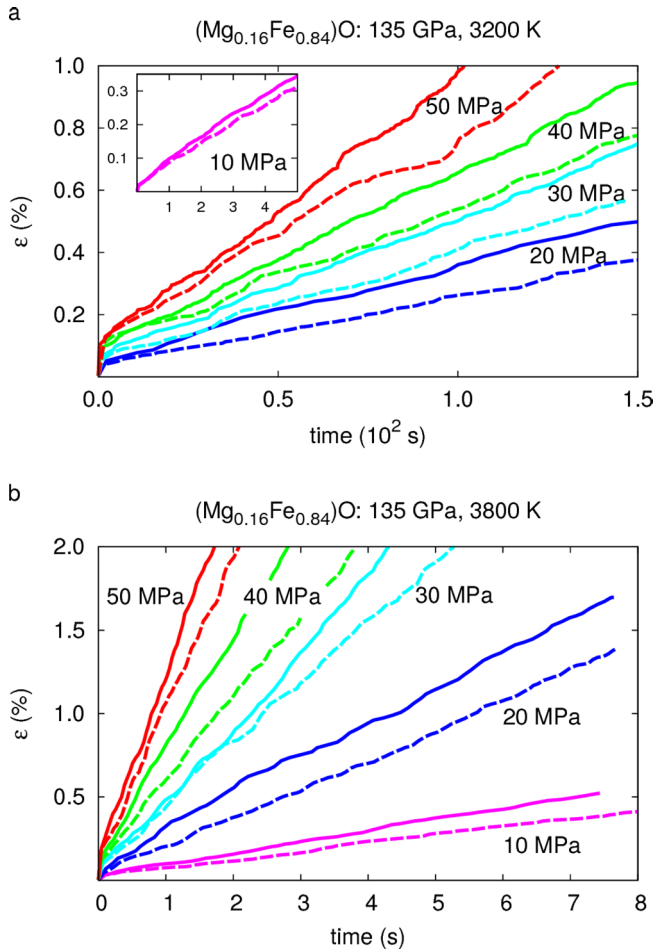
a

b

Fig. 7. Strain as a function of time for $(Mg_{0.16}Fe_{0.84})O$ magnesiowüstite at 135 GPa and 3200 K (a) and at 3800 K (b); from 10 to 50 MPa of applied stress. The solid lines in a and b represent the same curves displayed in Fig. 2b and c, respectively. The dashed lines represent the results obtained by raising the shear modulus of 10% for the same simulations. In a, the inset shows the two cases for an applied stress of 10 MPa.

presence in ULVZs (Wicks et al., 2017), the presence of such a low viscosity solid phase in localized patches above the CMB should influence the dynamics of the region.

5. Implications

The major result of our DD calculations and diffusion estimates is the prediction that iron-rich (Mg,Fe)O (magnesiowüstite) has a very

low viscosity relative to iron-poor (Mg,Fe)O (ferropericlase) at CMB conditions (Fig. 6). Therefore, to assess the influence of low viscosity magnesiowüstite on the dynamics of the lowermost mantle we revisit the proposal that the sound velocities of an assemblage containing magnesiowüstite can explain a suite of seismic observations (Wicks et al., 2010, 2017) and topography (Bower et al., 2011) of ULVZs.

5.1. Geodynamic model

The geodynamic model is described in detail in Bower et al. (2011). We use CitcomS (Moresi et al., 2014) to solve the equations of mass, momentum, and energy conservation in cylindrical geometry for a small region near the CMB (23 degrees by 488 km). The model includes a chemically-distinct material that has a larger intrinsic density than ambient mantle to model the iron-rich assemblage that forms the ULVZ. The larger intrinsic density is defined by a fraction of magnesiowüstite coexisting with the silicate mantle which can explain seismic wave speed reductions (Wicks et al., 2017). We now account for the viscosity reduction of Mw-bearing assemblages by reducing the intrinsic viscosity of the chemically-distinct material (ULVZ) relative to ambient mantle. The viscosity formulation therefore includes a compositional prefactor η_C in comparison to Eq. (8) in Bower et al. (2011):

$$\eta(C, T) = \eta_C exp(-ln(10^q)T_\eta) \tag{9}$$

where η is viscosity, η_C compositional prefactor, q order of magnitude viscosity contrast due to temperature (relates to activation energy), and T_η the non-dimensional temperature.

We select $\eta_C = 1$ for ambient mantle (C = 0) and $\eta_C = 0.1$ for ULVZ material (C = 1), which ensures a discernible effect of composition versus temperature on the flow pattern and hence the resulting geometry of the ULVZ. Since the ULVZ is not composed exclusively of $(Mg_{0.16},Fe_{0.84})O$ (Wicks et al., 2010; Bower et al., 2011; Wicks et al., 2017), it would be both physically unreasonable and numerically intractable to prescribe the total 10 orders of magnitude viscosity contrast between magnesiowüstite (component of ULVZ material) and ferropericlase (component of ambient mantle) (Fig. 6). Rather, the compositional prefactor extends the total viscosity range of the model to 4 orders of magnitude since $q = 3$. Other model parameters are the same as Bower et al. (2011) to enable a direct comparison of results.

Our new set of calculations prescribe an initial chemical layer thickness $d_{ch} = 4$ km at the base of the model, which was previously found to produce ULVZs that have reliefs within the mid-range of seismic predictions (Fig. 8C, 9C in Bower et al., 2011). We apply an isothermal and free-slip top boundary condition (referred to as "impermeable cases" in Bower et al., 2011). The buoyancy number B is non-dimensional and quantifies the intrinsic density contrast of the chemically-distinct material (ULVZ) relative to ambient mantle (*i.e.*, $\Delta\rho_{ch}/\rho$). We choose $B = 0.75, 1, 1.25, 2, 4$, and 6 (Table 5).

Table 4

Strain rates of magnesiowüstite at 135 GPa and at 3200 K and 3800 K for different applied stresses σ. The results obtained by raising the shear modulus μ of 10% are also shown, together with the calculated difference with respect to the original ones. [a]In this case μ is equal to 100 and 96 GPa for the cases at 3200 and 3800 K, respectively (*cf.* Table 1), while [b]the values of μ here are raised by 10% (resulting in 110 and 105.6 GPa, respectively).

	3200 K			3800 K		
	$\dot{\varepsilon}$ (s^{-1})			$\dot{\varepsilon}$ (s^{-1})		
σ (MPa)	μ^a	$\mu+10\%^b$	Ratio (%)	μ^a	$\mu+10\%^b$	Ratio (%)
10	$8.2 \cdot 10^{-6}$	$5.9 \cdot 10^{-6}$	28	$6.6 \cdot 10^{-4}$	$4.9 \cdot 10^{-4}$	26
20	$2.9 \cdot 10^{-5}$	$2.3 \cdot 10^{-5}$	21	$2.1 \cdot 10^{-3}$	$1.5 \cdot 10^{-3}$	28
30	$4.5 \cdot 10^{-5}$	$3.5 \cdot 10^{-5}$	23	$4.6 \cdot 10^{-3}$	$3.6 \cdot 10^{-3}$	22
40	$6.2 \cdot 10^{-5}$	$4.8 \cdot 10^{-5}$	22	$6.8 \cdot 10^{-3}$	$4.9 \cdot 10^{-3}$	28
50	$8.8 \cdot 10^{-5}$	$6.9 \cdot 10^{-5}$	22	$1.1 \cdot 10^{-2}$	$8.7 \cdot 10^{-3}$	21

Table 5
Relief H (km), half-width $W_{1/2}$ (km), and aspect ratio ($A = H/W_{1/2}$) for cases with (this study) and without (Bower et al., 2011) an intrinsic viscosity reduction for ULVZ material. Differences (%) are computed for the case with the ULVZ viscosity reduction relative to the case without the reduction. B is buoyancy number and the initial chemical layer thickness for all cases is d_{ch} = 4 km.

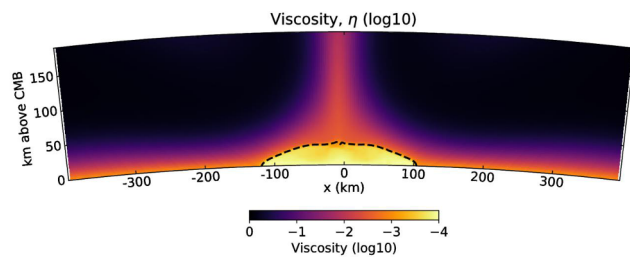| Case	B	No ULVZ reduction			With ULVZ reduction			Difference (%)		
		H	$W_{1/2}$	A	H	$W_{1/2}$	A	H	$W_{1/2}$	A
1	0.75	39	87	0.45	35	102	0.34	−10	18	−24
2	1.00	38	100	0.38	31	111	0.28	−20	11	−26
3	1.25	32	109	0.29	28	122	0.23	−12	12	−21
4	2.00	28	132	0.21	23	145	0.16	−19	10	−24
5	4.00	20	179	0.11	18	202	0.09	−9	13	−18
6	6.00	17	227	0.07	15	260	0.06	−10	15	−14

Fig. 8. Case 2 ($B = 1$) shows that a ULVZ containing iron-rich (Mg,Fe)O has lower intrinsic viscosity than ambient mantle, which influences the morphology of the ULVZ (see Table 5 and text). The ULVZ is bounded at the CMB by the black dashed line.

5.2. Morphology of ULVZs with low viscosity magnesiowüstite

We quantify the morphology of the ULVZ at steady-state by the relief H, defined as the 95% percentile of its height above the CMB, and half-width $W_{1/2}$, defined as half of its maximum (angular) footprint on the CMB. Table 5 shows the results for cases computed with (this study) and without (Bower et al., 2011) an intrinsic viscosity reduction for ULVZ material. An intrinsic viscosity reduction produces flatter ULVZs than predicted in models that do not consider the rheology of iron-rich (Mg,Fe)O; heights decrease by 10–20% and half-widths increase by 10–18% which results in aspect ratios decreasing by 14–26% (Table 5). This is because the intrinsic reduction in the viscosity of the ULVZ further decouples the ULVZ from the exterior flow in addition to the temperature-dependence of viscosity (Fig. 8). The tractions on the boundaries of the ULVZ are reduced, which means the exterior flow is less dominant in supporting the intrinsically dense ULVZ above the CMB. Rather, the ULVZ slumps to a greater extent due to its intrinsic density contrast.

Hence, an implication of comparatively weak magnesiowüstite is that less iron-rich (Mg,Fe)O needs to be incorporated into the ULVZ assemblage to account for the relief of a particular ULVZ. This is because both reducing the viscosity of the ULVZ material and increasing its intrinsic density contrast results in a flatter ULVZ that is characterized by both reduced height and greater width. For example, the B = 1 scenario ($\Delta\rho_{ch}/\rho$ = 1.5%) corresponds to the inclusion of around 3 vol% magnesiowüstite into the mantle assemblage at CMB conditions, with the range depending upon the actual phase assemblage and iron partitioning (*e.g.*, Bower et al., 2011, Wicks et al., 2017). Alternatively, another class of lowermost mantle seismic features could be explained by the presence of low viscosity magnesiowüstite. Kanamori (1967) and Buchbinder and Poupinet (1973) suggest that a thin core-mantle transition zone (CMTZ) could produce additional waveform complexity rather than a discontinuity, and further seismic studies indicate that a CMTZ of less than 4 km thick could be an alternative explanation for some ULVZs (*e.g.*, Vidale and Benz, 1992).

6. Conclusions

Dislocation dynamics simulations have been used to explore the dislocation creep behavior of (Mg,Fe)O ferropericlase and magnesiowüstite at D″ conditions. Upon retrieving the creep strain rates at different temperatures, pressures and applied stresses, we find that the viscosity of magnesiowüstite is reduced by about 10 orders of magnitude at the core-mantle boundary. By exploring the effects of an estimated viscosity contrast of a magnesiowüstite-bearing layer at the CMB, lower concentrations of magnesiowüstite would be required to explain the topographic relief reported in some ULVZ locations. However, thinner seismic features, such as the core-mantle transition zone, could host magnesiowüstite. In either of these cases, the recent findings that magnesiowüstite may have twice the shear wave anisotropy of postperovskite (Finkelstein et al., 2018) suggests that the presence of only small amounts of magnesiowüstite may significantly alter the characteristics of the core-mantle boundary.

References

Ando, K., Kurokawa, Y., Oishi, Y., 1983. Oxygen self-diffusion in Fe-doped MgO single crystals. J. Chem. Phys. 78, 6890–6892. https://doi.org/10.1063/1.444635.

Amodeo, J., Devincre, B., Carrez, P., Cordier, P., 2014. Dislocation reactions, plastic anisotropy and forest strengthening in MgO at high temperature. Mech. Mat. 71, 62–73.

Andrault, D., Pesce, G., Bouhifd, M.A., Bolfan-Casanova, N., Hénot, J.-M., Mezouar, M., 2014. Melting of subducted basalt at the core–mantle boundary. Science 344 (6186), 892–895.

Barr, L.W., Morrison, J.A., Schroeder, P.A., 1965. Anion diffusion in crystals of NaCl. J. Appl. Phys. 36 (2), 624–631.

Benzerga, A.A., Bréchet, Y., Needleman, A., Van der Giessen, E., 2003. Incorporating three-dimensional mechanisms into two-dimensional dislocation dynamics. Model. Simul. Mater. Sci. 12 (1), 159.

Boioli, F., Carrez, P., Cordier, P., Devincre, B., Marquille, M., 2015a. Modeling the creep properties of olivine by 2.5-D dislocation dynamics simulations. Phys. Rev. B 92 (1), 014115. https://doi.org/10.1103/PhysRevB.92.014115.

Boioli, F., Tommasi, A., Cordier, P., Demouchy, S., Mussi, A., 2015b. Steady state and low stresses in the lithospheric mantle inferred from dislocation modeling of creep in olivine. Earth Planet. Sci. Lett. 432, 232–242. https://doi.org/10.1016/j.epsl.2015.10.01.

Bower, D.J., Wicks, J.K., Gurnis, M., Jackson, J.M., 2011. A geodynamic and mineral physics model of a solid-state ultra-low velocity zone. Earth Planet. Sci. Lett. 303 (3–4), 193–202. https://doi.org/10.1016/j.epsl.2010.12035.

Buchbinder, G., Poupinet, G., 1973. Problems related to PcP and the core–mantle boundary illustrated by two nuclear events. Bull. Seismol. Soc. Am. 63, 2047–2070.

Caillard, D., Martin, J.L., 2003. Thermally Activated Mechanisms in Crystal Plasticity 8. Elsevier.

Carrez, P., Cordier, P., Devincre, B., Kubin, L.P., 2005. Dislocation reactions and junctions in MgO. Mat. Sci. Eng. A 400, 325–328.

Chen, W.K., Jackson, R.A., 1969. Oxygen self-diffusion in undoped and doped cobaltous oxide. J. Phys. Chem. Solids 30 (6), 1309–1314.

Cohen, R.E., Weitz, J.S., 1998. The melting curve and premelting of MgO. Geoph. Monog. Series 185–196.

Cordier, P., Amodeo, J., Carrez, P., 2012. Modelling the rheology of MgO under Earth's mantle pressure, temperature and strain rates. Nature 481 (7380), 177–180.

Deng, J., Lee, K.K.M., 2017. Viscosity jump in the lower mantle inferred from melting curves of ferropericlase. Nat. Commun. 8, 1997.

Devincre, B., Kubin, L., Hoc, T., 2006. Physical analyses of crystal plasticity by DD simulations. Scripta Mater. 54 (5), 741–746.

Dorfman, S.M., Duffy, T.S., 2014. Effect of Fe-enrichment on seismic properties of perovskite and post-perovskite in the deep lower mantle. Geophys. J. Int. 197, 910–919.

Du, Z., Lee, K.K.M., 2014. High-pressure melting of MgO from (Mg, Fe)O solid solutions. Geophys. Res. Lett. 41, 8061–8066.

Durinck, J., Devincre, B., Kubin, L., Cordier, P., 2007. Modeling the plastic deformation of olivine by dislocation dynamics simulations. Am. Mineral. 92 (8–9), 1346–1357.

Fat'yanov, O.V., Asimow, P.D., 2014. MgO melting curve constraints from shock temperature and rarefaction overtake measurements in samples preheated to 2300 K. J. Phys. Conf. Ser. 500 (6), 062003.

Finkelstein, G.J., Jackson, J.M., Said, A., Alatas, A., Leu, B.M., Sturhahn, W., Toellner, T.S., 2018. Strongly anisotropic magnesiowüstite in Earth's lower mantle. J. Geophys. Res.-Sol. Earth 123. https://doi.org/10.1029/2017JB015349, in press.

Fiquet, G., Auzende, A.L., Siebert, J., Corgne, A., Bureau, H., Ozawa, H., Garbarino, G., 2010. Melting of peridotite to 140 Gigapascals. Science 329 (5998), 1516–1518.

Fischer, R.A., Campbell, A.J., 2010. High-pressure melting of wüstite. Am. Mineral. 95, 1473–1477.

Fischer, R.A., Campbell, A.J., Shofner, G.A., Lord, O.T., Dera, P., Prakapenka, V.B., 2011. Equation of state and phase diagram of FeO. Earth Planet. Sci. Lett. 304, 496–502.

Frost, D.A., Garnero, E.J., Rost, S., 2018. Dynamical links between small- and large-scale mantle heterogeneity: seismological evidence. Earth Planet. Sci. Lett. 482, 135–146.

Fu, S., Yang, J., Zhang, Y., Liu, J., Greenberg, E., Prakapenka, V.B., Okuchi, T., Lin, J.-F., 2018. Melting behavior of the lower-mantle ferropericlase across the spin crossover: Implication for the ultra-low velocity zones at the lowermost mantle. Earth Planet. Sci. Lett. 503, 1–9.

Fuller, R.G., 1966. Diffusion of the chlorine ion in potassium chloride. Physi. Rev. 142 (2), 524.

Garnero, E.J., Helmberger, D.V., 1995. A very slow basal layer underlying large-scale low-velocity anomalies in the lower mantle beneath the pacific – evidence from core phases. Phys. Earth Planet. Int. 91 (1–3), 161–176.

Gassner, A., Thomas, C., Krüger, F., Weber, F., 2015. Probing the core-mantle boundary beneath Europe and Western Eurasia: a detailed study using PcP. Phys. Earth Planet. Int. 246, 9–24.

Gómez-García, D., Devincre, B., Kubin, L.P., 2006. Dislocation patterns and the similitude principle: 2.5D mesoscale simulations. Phys. Rev. Lett. 96 (12), 125503.

Hirth, J.P., Lothe, J., 1992. Theory of Dislocations. Wiley.

Hernlund, J.W., Tackley, P.J., 2007. Some dynamical consequences of partial melting in Earth's deep mantle. Phys. Earth Planet. Int. 162 (1–2), 149–163.

Hernlund, J.W., Jellinek, A.M., 2010. Dynamics and structure of a stirred partially molten ultralow-velocity zone. Earth Planet. Sci. Lett. 296 (1–2), 1–8.

Hutko, A., Lay, T., Revenaugh, J., 2009. Localized double-array stacking analysis of PcP: D″ and ULVZ structure beneath the Cocos plate, Mexico, central Pacific, and north Pacific. Phys. Earth Planet. Int. 173 (1–2), 60–74.

Immoor, J., Marquardt, H., Miyagi, L., Lin, F., Speziale, S., Merkel, S., Buchen, J., Kurnosov, A., Liermann, H.-P., 2018. Evidence for {100} < 011 > slip in ferropericlase in Earth's lower mantle from high-pressure/high-temperature experiments. Earth Planet. Sci. Lett. 489, 251–257.

Ita, J., Cohen, R.E., 1997. Effects of pressure on diffusion and vacancy formation in MgO from nonempirical free-energy integrations. Phys. Rev. Lett. 79 (17), 3198.

Kanamori, H., 1967. Spectrum of P and PcP in relation to the mantle-core boundary and attenuation in the mantle. J. Geophys. Res. 72, 559–571.

Kato, C., Hirose, K., Nomura, R., Ballmer, M.D., Miyake, A., Ohishi, Y., 2016. Melting in the FeO-SiO$_2$ system to deep lower-mantle pressures: Implications for subducted Banded Iron Formations. Earth Planet. Sci. Lett. 440, 56–61.

Keralavarma, S.M., Cagin, T., Arsenlis, A., Benzerga, A.A., 2012. Power-law creep from discrete dislocation dynamics. Phys. Rev. Lett. 109 (26), 265504.

Knittle, E., Jeanloz, R., 1991a. Earth's core-mantle boundary – results of experiments at high-pressures and temperatures. Science 251, 1483–11443.

Knittle, E., Jeanloz, R., 1991b. The high-pressure phase diagram of Fe$_{0.94}$O: A possible constituent of the Earth's core. J. Geophys. Res. 96, 16169–16180.

Komabayashi, T., 2014. Thermodynamics of melting relations in the system Fe-FeO at high pressure: implications for oxygen in the Earth's core. J. Geophys. Res.-Sol. Ea. 119, 4164–4177.

Labrosse, S., Hernlund, J.W., Coltice, N., 2007. A crystallizing dense magma ocean at the base of the Earth's mantle. Nature 450 (7171), 866–869.

Lay, T., Hernlund, J., Buffett, B.A., 2008. Core-mantle boundary heat flow. Nat. Geosci. 1 (1), 25–32.

Li, M., McNamara, A.K., Garnero, E.J., Yu, S., 2017. Compositionally-distinct ultra-low velocity zones on Earth's core-mantle boundary. Nat. Commun. 8, 177.

Lin, J.-F., Wenk, H.-R., Voltolini, M., Speziale, S., Shu, J., Duffy, T.S., 2009. Deformation of lower-mantle ferropericlase (Mg, Fe)O across the electronic spin transition. Phys. Chem. Miner. 36, 585–592.

Liu, J., Hu, Q., Kim, D.Y., Wu, Z., Wang, W., Xiao, Y., Chow, P., Meng, Y., Prakapenka, V.B., Mao, H.-K., Mao, W.L., 2017. Hydrogen-bearing iron peroxide and the origin of ultralow-velocity zones. Nature 551, 494.

Mao, W.L., Shen, G., Prakapenka, V., Meng, Y., Campbell, A.J., Heinz, D.L., Shu, J., Hemley, R.J., Mao, H.-K., 2004. Ferromagnesium postperovskite silicates in the D″ layer of the Earth. P. Natl. A. Sci. 101 (45), 15867–15869.

Marquardt, H., Miyagi, L., 2015. Slab stagnation in the shallow lower mantle linked to an increase in mantle viscosity. Nat. Geosci. 8 (4), 311–314.

Moresi, L.S. Zhong, L. Han, C. Conrad, M. Gurnis, E. Choi, P. Thoutireddy, V. Manea, A. McNamara, T. Becker, W. Leng, Armendariz, L., 2014. Citcoms v3.3.1 [software], Computational Infrastructure for Geodynamics. URL: https://geodynamics.org/cig/software/citcoms/.

Muir, J.M.R., Brodholt, J.P., 2015. Elastic properties of ferropericlase at lower mantle conditions and its relevance to ULVZs. Earth Planet. Sci. Lett. 417, 40–48.

Nomura, R., Hirose, K., Uesugi, K., Ohishi, Y., Tsuchiyama, A., Miyake, A., Ueno, Y., 2014. Low core-mantle boundary temperature inferred from the solidus of pyrolite. Science 343 (6170), 522–525.

Oishi, Y., Ando, K., Kurokawa, H., Hiro, Y., 1983. Oxygen Self-Diffusion in MgO Single Crystals. J. Am. Ceram. Soc. 66 (4), C60–C62.

Ozawa, H., Hirose, K., Ohta, K., Ishii, H., Hiraoka, N., Ohishi, Y., Seto, Y., 2011. Spin crossover, structural change, and metallization in NiAs-type FeO at high pressure. Phys. Rev. B 84, 134417.

Pradhan, G.K., Fiquet, G., Siebert, J., Auzende, A.-A., Morard, G., Antonangeli, D., Garbarino, G., 2015. Melting of MORB at core-mantle boundary. Earth Planet. Sci. Lett. 431, 247–255.

Reali, R., Boioli, F., Gouriet, K., Carrez, P., Devincre, B., Cordier, P., 2017. Modeling plasticity of MgO by 2.5D dislocation dynamics simulations. Mat. Sci. Eng. A 690, 52–61. https://doi.org/10.1016/j.msea.2017.02.092.

Reaman, D.M., Colijn, H.O., Yang, F., Hauser, A.J., Panero, W.R., 2012. Interdiffusion of Earth's core materials to 65 GPa and 2200 K. Earth Planet. Sci. Lett. 349, 8–14. https://doi.org/10.1016/j.epsl.2012.06.053.

Revenaugh, J., Meyer, R., 1997. Seismic evidence of partial melt within a possibly ubiquitous low-velocity layer at the base of the mantle. Science 277, 670–673.

Rost, S., Garnero, E.J., Williams, Q., 2006. Fine-scale ultralow-velocity zone structure from high-frequency seismic array data. J. Geophys. Res. 111, B09310.

Rost, S., 2013. Deep earth: core-mantle boundary landscapes. Nat. Geosci. 6, 89–90.

Sakai, T., Ohtani, E., Terasaki, H., Miyahara, M., Nishijima, M., Hirao, N., Ohishi, Y., Sata, N., 2010. Fe-Mg partitioning between post-perovskite and ferropericlase in the lowermost mantle. Phys. Chem. Min. 37 (7), 487–496.

Shen, G., Lazor, P., Saxena, S.K., 1993. Melting of wüstite and iron up to pressures of 600 kbar. Phys. Chem. Minerals 20, 91–96.

Singh, R.P., Singh, M.P., Singh, R.K., 2008. Acoustical dissipation due to phonon-phonon interaction, thermoelastic loss and dislocation damping in MnO and CoO. Proceedings of Meetings on Acoustics 155ASA. ASA (Vol. 4, No. 1, p. 045006).

Solomatova, N.V., Jackson, J.M., Sturhahn, W., Wicks, J.K., Zhao, J., Toellner, T.S., Kalkan, B., Steinhardt, W.M., 2016. Equation of state and spin crossover of (Mg, Fe)O at high pressure, with implications for explaining topographic relief at the core-mantle boundary. Am. Mineral. 101 (5), 1084–1093.

Speziale, S., Milner, A., Lee, V.E., Clark, S.M., Pasternak, M.P., Jeanloz, R., 2005. Iron spin transition in Earth's mantle. Proc. Natl. Acad. Sci. 102, 17918–17922.

Sturhahn, W., Jackson, J.M., Lin, J.F., 2005. The spin state of iron in minerals of Earth's lower mantle. Geophys. Res. Lett. 32 (12), L12307.

Sun, D., Helmberger, D.V., Jackson, J.M., Clayton, R.W., Bower, D.J., 2013. Rolling hills on the core-mantle boundary. Earth Planet. Sci. Lett. 361, 333–342. https://doi.org/10.1016/j.epsl.2012.10.027.

Tateno, S., Hirose, K., Ohishi, Y., 2014. Melting experiments on peridotite to lowermost mantle conditions. J. Geophys. Res.-Sol. Eaeth 119 (6), 4684–4694.

Thorne, M.S., Garnero, E.J., Jahnke, G., Igel, H., McNamara, A.K., 2013. Mega ultra low velocity zone and mantle flow. Earth Planet. Sci. Lett. 364, 59–67.

Tsuchiya, T., Wentzcovitch, R.M., da Silva, C.R., de Gironcoli, S., 2006. Spin transition in magnesiowüstite in Earth's lower mantle. Phys. Rev. Lett. 96 (19), 198501.

Van Orman, J.A., Fei, Y., Hauri, E.H., Wang, J., 2003. Diffusion in MgO at high pressures: constraints on deformation mechanisms and chemical transport at the core-mantle boundary. Geophys. Res. Lett. 30 (2).

Van Orman, J.A., Crispin, K., 2010. Diffusion in oxides. Rev. Mineral. Geochem. 72 (2010), 757–825. https://doi.org/10.2109/jcersj1950.74.851_215.

Vidale, J.E., Benz, H.M., 1992. A sharp and flat section of the core mantle boundary. Nature 359, 627–629.

Wicks, J.K., Jackson, J.M., Sturhahn, W., 2010. Very low sound velocities in iron-rich (Mg, Fe)O: implications for the core-mantle boundary region. Geophys. Res. Lett. 37, L15304.

Wicks, J.K., Jackson, J.M., Sturhahn, W., Zhuravlev, K.K., Prakapenka, V., 2015. The thermal equation of state and stability of iron-rich (Mg, Fe)O. Phys. Earth Planet. Int. 249, 28–42.

Wicks, J.K., Jackson, J.M., Sturhahn, W., Zhang, D., 2017. Sound velocity and density of magnesiowüstites: implications for ultralow-velocity zone topography. In: Geophys. Res. Lett.pp. 44.

Williams, Q., Garnero, E., 1996. Seismic evidence for partial melt at the base of the

mantle. Science 273, 1528–1530.

Wu, P., Eriksson, G., Pelton, A.D., 1993. Critical evaluation and optimization of the thermodynamic properties and phase diagrams of the CaO–FeO, CaO–MgO, CaO–MnO, FeO–MgO, FeO–MnO, and MgO–MnO systems. J. Am. Ceram. So. 76 (8), 2065–2075.

Wu, Z., Wentzcovitch, R.M., 2014. Spin crossover in ferropericlase and velocity heterogeneities in the lower mantle. Proc. Natl. A. Sci. 111 (29), 10468–10472.

Yamaguchi, S., Someno, M., 1982. The tracer diffusivity of oxygen in Wüstite and Cobaltous oxide. T. Jpn. I. Met. 23 (5), 259–266.

Yamazaki, D., Karato, S., 2001. Some mineral physics constraints on the rheology and geothermal structure of Earth's lower mantle. Am. Mineral. 86, 385–391.

Yang, M.H., Flynn, C.P., 1994. Intrinsic diffusion properties of an oxide: MgO. Phys. Rev. Lett. 73, 1809–1812.

Yang, M.H., Flynn, C.P., 1996. Ca^{2+} and $^{18}O^{2-}$ diffusion in ultrapure MgO. J. Phys. Condens. Matter 8, L279–L283.

Yu, S., Garnero, E.J., 2018. Ultra-low velocity zone locations: a global assessment. Geochem. Geophys. Geosys. 19 (2), 396–414. https://doi.org/10.1002/2017GC007281.

Zerr, A., Boehler, R., 1994. Constraints on the melting temperature of the lower mantle from high-pressure experiments on MgO and magnesiowüstite. Nature 371 (6497), 506.

Zhang, L., Fei, Y., 2008. Melting behavior of (Mg, Fe)O solid solutions at high pressure. Geophys. Res. Lett. 35, L13302.

Zhang, D., Jackson, J.M., Zhao, J., Sturhahn, W., Alp, E.E., Hu, M., Toellner, T.S., Murphy, C.A., Prakapenka, V., 2016. Temperature of Earth's core constrained from melting of Fe and $Fe_{0.9}Ni_{0.1}$ at high pressures. Earth Planet. Sci. Lett. 447, 72–83.

Zhang, B., Ni, S., Sun, D., Shen, Z., Jackson, J.M., Wu, W., 2018. Constraints on small-scale heterogeneity in the lowermost mantle from observations of near podal PcP precursors. Earth Planet. Sci. Lett. 489, 267–276.